Structures 70 (2024) 107548

Contents lists available at ScienceDirect

Structures

journal homepage: www.elsevier.com/locate/structures

Dynamic performance investigations of a full-scale unanchored thin-walled steel fluid storage tank via shake table tests

Seyed Ehsan Aghakouchaki Hosseini *, Sherif Beskhyroun

Department of Built Environment Engineering, Faculty of Design and Creative Technologies, School of Future Environments, Auckland University of Technology (AUT), 1010 Auckland, New Zealand

ARTICLE INFO

Keywords:
Fluid storage tanks
Shake table test
Simplified mechanical model
Signal processing

ABSTRACT

Theoretical models proposed in the literature and seismic design codes make the basis of analysis and the design procedures of fluid storage tanks. These models are derived based on many simplified and approximate assumptions. Under realistic conditions, however, different factors cause violation of these assumptions, causing the fluid flow and fluid–structure interaction (FSI) to diverge from theories. In this research work, 38 swept-sine tests and 63 seismic ground motions were applied to a full-scale highly flexible unanchored thin-walled stainless steel fluid tank. The experimental natural frequencies of the system for three different aspect ratios of 2.1, 2.8, and 3.5 were calculated and compared with the theoretical ones. Damping ratios for different modes were calculated using the half-power bandwidth analysis. Experimental results revealed discrepancies between the theoretical and experimentally detected natural frequencies, especially for the convective mode. Closer matches were found for the aspect ratios of 2.8 and 3.5, for the impulsive mode. Acceleration amplification factors at different heights of the shell were calculated which showed a nonlinear behaviour with a descending trend from the base to the mid-height and then an ascending one towards the fluid surface. Maximum acceleration amplification factor occurred at the surface of the fluid. The axial strains around the base are maximum and decrease bi-linearly towards the upper heights of the shell. Effects of the input excitation frequency content over the structural responses of the system were examined. Frequency characteristics of the input excitation considerably affected the maximum acceleration amplification factors and axial strains in the shell.

1. Introduction

Thin-walled stainless steel fluid storage tanks are used in a variety of applications and industries including wineries, dairy products industries, water storage purposes, and petrochemical industries, to name but a few. Related industries were heavily damaged financially during past earthquakes. Examples of past occurrences which resulted in massive losses are the 2010 Maul earthquake in Chile [1], the 2011 Christchurch [2], the 2013 Marlborough [3], and the 2016 Kaikōura [4] earthquakes in New Zealand, the 2012 Emilia earthquake in Italy [5], the 2014 Napa earthquake in California [6], and the 1989 Loma Prieta earthquake [7], among others. Due to the huge inflicted losses caused by these events, it is imperative to understand the way these structures will behave realistically during seismic events. This will help modify the current analysis procedures for more accurate designs of these structures to avoid future catastrophes.

The main approaches that are applied for the analysis and design of these tanks are based on the equivalent mechanical models proposed in the literature. Mostly used techniques for this purpose include those presented by Housner [8,9], Haroun [10], Veletsos [11], and Malhotra [12], among others, which form the design basis of many seismic codes in different parts of the world including American Petroleum Institute (API) 650 [13], Eurocode 8, Part 4 [14], and the New Zealand Society for Earthquake Engineering (NZSEE) [15]. These simplified techniques were substantial efforts to express a highly complicated phenomenon in these structures which is the fluid–structure interaction (FSI) in a closed-form mathematical expression that could be easily applied for calculations. However, there are many approximate and simplified assumptions behind these mechanical models, the most important of which are irrotationality and small-amplitude surface fluid oscillations when formulating the Navier–Stokes equations. A comprehensive literature review conducted by the authors studied in detail a variety of dynamic modelling techniques proposed for these structural systems [16], different types of damages observed in past seismic events, different methodologies proposed in the literature for analysing the fluid tanks, the assumptions made for each technique, and the modified proposed models. Among the crucial factors that cause

* Corresponding author.
E-mail addresses: ehsan.hosseini@autuni.ac.nz (S.E.A. Hosseini), sherif.beskhyroun@aut.ac.nz (S. Beskhyroun).

https://doi.org/10.1016/j.istruc.2024.107548
Received 27 March 2024; Received in revised form 10 October 2024; Accepted 11 October 2024
Available online 24 October 2024

the violation of these assumptions and substantial differences between mathematical results, and what occurs in practice, the below items can be mentioned:

- flexibility of the tank shell in thin-walled steel tanks [17,18].
- the fixity conditions of the tank base plate to the ground or foundation [19].
- the rotational and chaotic behaviour of the surface water oscillations [20].
- interaction between the underlying soil and the tank [21].
- characteristics of the ground motion, including duration, mechanism, frequency content, and amplitude [22].
- second order (P-Δ) and material nonlinearities, as well as uncertainties in properties of the tank materials and geometry, contained liquid, and excitation [23,24] and finally,
- fluid flow characteristics such as multi-phase flow and Coriolis effects [25].

These approximations when formulating the mechanical models will result in inaccuracies in estimating the structural characteristics of fluid tanks including natural frequencies of the impulsive and convective modes which are the two dominant vibrational modes in these structures. Stainless-steel fluid storage tanks have a very thin shell and are commonly used for the storage of wine, water, dairy products, etc. These tanks are either legged or flat-based. In terms of connection to the ground or foundation, they could be anchored or unanchored. Studies have shown that these structures are one of the main elements of wineries that are vulnerable to damage even in regions that have a low seismic risk [26].

Recently, some research efforts were dedicated to a better understanding of the seismic behaviour of fluid storage tanks and modifying initial simplified mechanical models (SMMs), either numerically or experimentally [16]. A series of experimental tests and corresponding numerical validations have been performed over double-layer liquefied natural gas (LNG) storage tanks [27,28]. Liu et al. [29] investigated the effects of FSI and the validity of the small amplitude linearized fluid motions theory of the liquid surface in a liquefied natural gas (LNG) storage tank made of an inner steel cylindrical tank and an outer reinforced concrete tank. They reported significant discrepancies between their experimental results and those presented by the SMM of Housner [9] under seismic excitations. Compagnoni and Curadelli [30] tested a flat-based steel cylindrical tank with a thickness of 1.5 mm using shake table excitations for aspect ratios of 0.5, 1.0, and 1.5. In their studies, comparisons between the finite element (FE) and the SMM results with that of experiments showed that the SMM underestimates the fluid surface maximum vertical displacement up to 35% while it overestimates the maximum base shear and overturning moment. Shake table tests over an aluminium tank were implemented for two cases of anchored and unanchored conditions by Ormeño et al. [31]. This tank model had a shell and base thickness of 3 mm. Shake table testing of a large-scale legged fluid storage tank with a shell thickness of 2 mm was conducted by Yazdanian et al. [32]. Shake table examinations over a legged stainless-steel cylindrical fluid tank were conducted by Reyes et al. [33] to study the performance of a new isolation system. Damage assessments of fluid tanks in previous seismic events have shown that the thickness of the shell, aspect ratio, and the characteristics of the ground excitation are among the most important factors that substantially contribute to the most common types of damage to these structures. These damage types include diamond shape and elephant foot buckling [4,18,34–36]. The seismic performance of self-supported cylindrical fluid tanks during the 2023 Turkey earthquakes was studied in [37]. In this work, typical types of damage that occurred to these tanks were mentioned as damage to the upper part of the shell due to the sloshing of the liquid and rupture at the location of the pipe connections.

The numerical investigations based on a coupled boundary element – finite element (BE-FE) analysis on the isolated tanks by researchers in [38] considered the wall flexibility as one of the important factors that affect the efficiency of the isolation system. In another research by Shekari [39], the effect of the frequency content and the predominant period of the base excitation on the seismic behaviour of base-isolated concrete rectangular liquid tanks were investigated using the BE-FE-BE method. In this study, two types of rigid and flexible tanks with thicknesses of the wall equal to 1.2 m and 0.6 m were considered. A simplified model for structural response estimation of a rectangular concrete fluid tank under earthquakes was proposed in [40] based on Lagrange's equation and combining the fundamental modes of a cantilever beam and a rectangular-ring-shaped frame structure. The thickness of the modelled tank in this study was considered as 1 m. In [41] a numerical FE analysis of the nonlinear behaviour of an unanchored cylindrical steel fluid tank was examined by considering the effects of the underlying soil. In this research, two types of tall and broad tanks with approximate wall thicknesses of around 15 mm were investigated. Their results showed that the structural responses and the hydrodynamic pressure are influenced by the base uplift and the soil flexibility. Dynamic behaviour of cylindrical ground-supported tanks considering the fluid–structure-soil interaction, under earthquakes with different frequency contents was numerically investigated in [42] using the discrete-time state–space approach. In this research, numerical investigations were conducted over a steel tank with a thickness of 25.4 mm. It was demonstrated that the frequency content of the base excitation is an influential factor in the seismic response of fluid tanks. Cui et al. [43] numerically investigated the effects of the flexibility of the tank shell on the seismic response of horizontal fluid tanks. They proposed a simplified mechanical model for dynamic response evaluation of flexible tanks and used a tank with a wall thickness of 12 mm for validation of their method. Their results showed the amplification of the tank's seismic responses due to the shell flexibility including the liquid dynamic peak pressure, among others, compared to that of the rigid tanks.

Researchers have utilized different excitation methods for the vibrational analysis of fluid storage tanks in literature. The contribution of the second convective mode in responses of rigid liquid storage tanks using wavelets was examined numerically in [44]. Wavelet analysis was used for numerical seismic response evaluation of base-isolated liquid storage tanks [45]. Sine and ricker wavelet excitation tests have been applied for shake table testing of a low-density polyethylene (LDPE) tank with a thickness of 4 mm [36]. Pulse tests by shake table were used for the same tank in [46] for free-vibration frequency determination of the fluid tank for rigid and flexible support conditions.

Compared to a considerable number of numerical investigations conducted on the dynamic behaviour modelling of fluid storage tanks in the literature, fewer experimental investigations have been conducted. Authors believe that experimental research on full-scale stainless steel unanchored circular cylindrical fluid tanks with very small thicknesses (as small as 0.5 mm investigated in this research) is rare in the literature. It is of paramount importance to truly understand the dynamic performance of such tanks in terms of their structural characteristics and how they behave under base excitations. It is noteworthy that shell thickness in stainless-steel tanks plays a pivotal role in the flexibility of the coupled fluid-tank system, and hence the dynamic characteristics of the structure including natural frequencies and damping ratios.

In this research work, experimental findings of shake table tests conducted over a thin-walled stainless steel cylindrical fluid storage tank are examined and discussed. The tested tank had a capacity of 1000 l and a very thin shell thickness of 0.5 mm. The very thin shell contributed to the highly flexible behaviour of the tank-liquid system. The fluid tank was set up over the shake table without any type of connection, allowing it to freely uplift under applied base excitations. This tank was tested for three different capacities of the tank, i.e. 50%, 70%, and 85% full, resulting in aspect ratios of 2.1, 2.8, and 3.5, respectively. Swept-sine excitation tests have been proved as simple and efficient means for natural frequency estimation of structures which offer robustness, rapidity, and stability, as well [47–49]. They also have found successful applications for structural health monitoring purposes [48,50]. Thus, to evaluate the dynamic performance of such a full-scale thin-walled stainless steel tank, two types of excitations including swept-sine tests with different frequency bands, durations, and amplitudes, and five seismic records of selected past devastating earthquakes were applied to the shake table. Applied seismic records had different characteristics including Near-fault, Far-fault, Pulse-like, and different mechanisms of Strike-Slip and Reverse-Oblique. These records were scaled to different intensities which were gradually increased to allow for a sufficient number of tests and data collection before the final collapse of the system. Since the tank was very thin and completely free for uplift motions, finally it collapsed through the formation of a crack in the base plate. Signal processing based on frequency domain analyses using Fast Fourier Transform (FFT), Power Spectral Density (PSD), Cross Power Spectral Density (CPSD), and time–frequency domain analyses using Short-time Fourier Transform (STFT) (Spectrogram) were applied to the experimental data using Signal Processing Toolbox in MATLAB R2023a [51] for data analysis. The aim of the data analysis was to extract the structural characteristics of the tank-liquid system including natural frequencies and damping ratios for such a highly flexible stainless-steel full-scale fluid storage tank. Additionally, the frequency content of the excitations and their effect on the developed responses of the tank were examined. Experimental results were compared to those of the theoretical model using the equivalent mechanical model mostly used in the seismic codes for the analysis and design of tanks. The results of analyses demonstrated how closely and well these two types of results match each other. Conducted comparative studies enabled a better understanding of the fluid tanks' seismic behaviour under actual ground motions compared to numerical simulations using simplified equations.

2. Experimental set-up

2.1. Installations, dimensions, and supporting frame

The investigated fluid storage tank was set over the unidirectional shake table in the Structural Engineering Laboratory of the Auckland University of Technology (AUT) as seen in Figs. 1 and 2. The shake table platform is a unidirectional table with dimensions of 4000 mm by 2896 mm and a maximum horizontal stroke of ± 200 mm, run by the Shore Western controller. The maximum payload of the table is 1 ton and it is capable of producing accelerations up to $2g$. As there were no connections from the tank base to the table, a supporting frame was provided as shown in Fig. 2. This supporting frame consists of steel columns and beams, timber beams, and a timber plate underneath the tank to avoid any kind of damage to the shake table and other apparatus in case of overturning, buckling, or rupture of the shell or base plate that could cause flow of water over the table. This tank was made of stainless steel of grade 304, had a capacity of 1000 l, and a height, diameter, and thickness equal to 1900 mm, 850 mm, and 0.5 mm, respectively. The tank was filled in three stages up to 50%, 70%, and 85% of its capacity with water to conduct tests.

2.2. Instrumentation

The fluid storage tank was instrumented according to Fig. 3. Different types of sensors including accelerometers, strain gauges, draw wires, and LVDTs were employed to measure structural responses of the system. These measurements include lateral accelerations and displacements of the shell, axial strains in the shell, and uplift of the tank base. Data acquisition was provided using the National Instruments Data Acquisition (NI DAQ) system for receiving and logging signals from the sensors. One accelerometer was attached to the shake table to measure the table's acceleration time history.

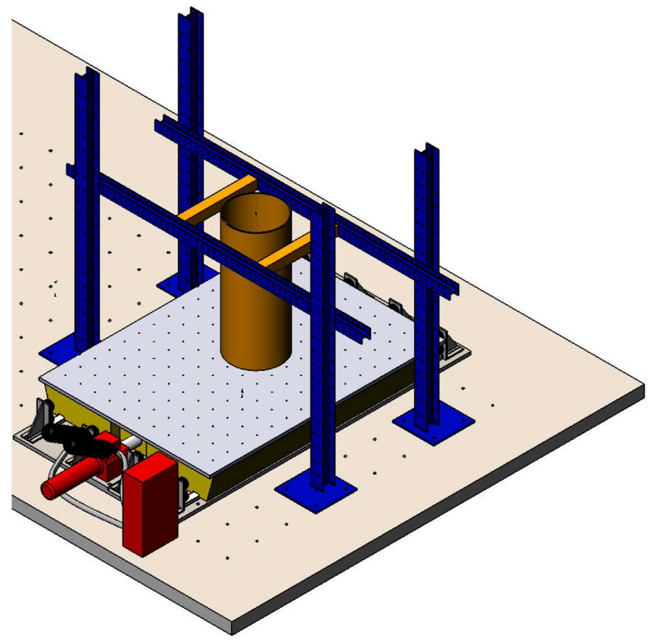

Fig. 1. Isogeometric perspective of the experimental set-up using SOLIDWORKS.

Fig. 2. Physical model of the tank and the supporting frame.

3. Base excitation tests

Two types of excitation were applied to the shake table including swept-sine tests and displacement time histories of five past historic ground motions. A total of 101 tests were conducted which consisted of 38 swept-sine tests and 63 seismic ground motion tests. More precise details of the conducted tests and base excitations can be found in Tables 1–3.

3.1. Swept-sine tests

Swept-sine excitation tests have demonstrated high performance and efficiency in vibration tests and structural health monitoring techniques in terms of simplicity, rapidity, robustness, and repeatability [47–50]. A swept-sine excitation with a linear frequency rate can be mathematically represented as Eq. (1),

$$A(t) = A_{amp} \sin\left[2\pi\left(f_0 t + \frac{\beta t^2}{2}\right) + \varphi_0\right] \quad (1)$$

$$\beta = \frac{f_f - f_0}{T} \quad (2)$$

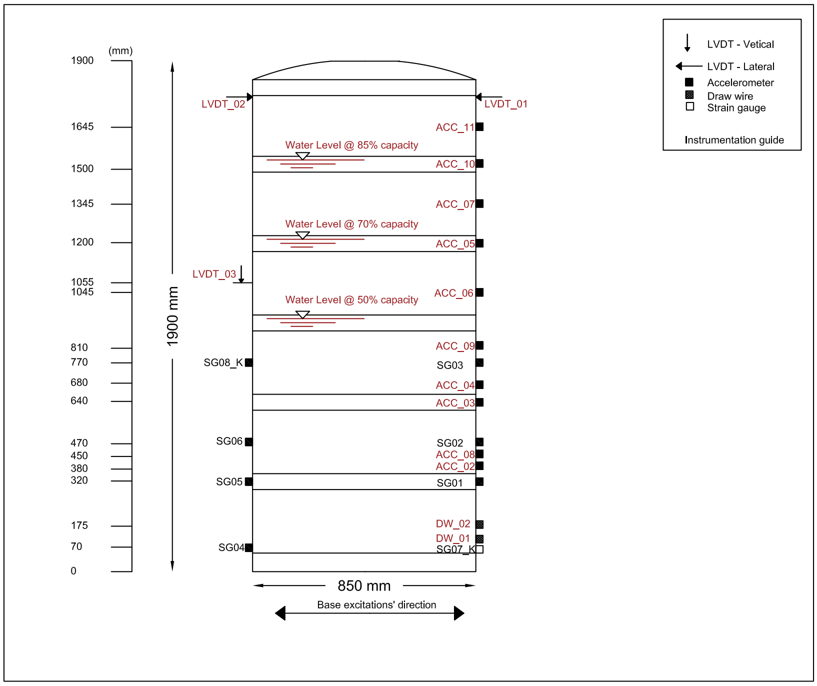

Fig. 3. Instrumentation of the fluid tank.

where A_{amp} is the amplitude of the swept-sine, f_0 is the initial frequency, f_f is the final frequency, T is the sweep duration, β is the sweep rate, and φ_0 is the initial phase.

In this study, each swept-sine test had a different frequency band, duration, and amplitude. The swept-sine tests were of linear type for the frequency of the sweep with constant amplitude. Each test was applied with a specific constant amplitude. Some of the tests were repeated up to three times to account for uncertainties and noise influences. The swept-sine tests were conducted for three different capacities of the tank, i.e. 50%, 70%, and 85% equivalent to aspect ratios of 2.1, 2.8, and 3.5, respectively. Accordingly, the frequency band of the swept-sine was regulated to target the natural frequencies of the system at specific ranges. The higher the values of the frequency band of the swept-sine test, the lower the displacement amplitude of the sweep was applied.

It was found that both the frequency values of the excitation and its amplitude had considerable influences on the vibratory behaviour of the system. However, the influence of the frequency values of excitation in exciting the fluid-tank system was found more influential than the displacement amplitude. Considering the very small shell thickness of the tank body, when the frequency of the excitation matched the resonant frequency of the system in each test, the tank started to vibrate terrifically. Therefore, as the dynamic behaviour of the tank was monitored visually in each test, it was managed to regulate the displacement amplitude of the next sweep test according to its frequency band values to avoid any unexpected damage and finish the test successfully. For some tests when it was found safe, for the same frequency band of the sweep, the amplitude value was increased in the next test to examine its effect on the responses of the tank. Reversely, in some tests, the sweep amplitude was decreased and the same test was repeated again. The duration of tests was selected as 60 s, 120 s, 240 s and 300 s. When targeting a specific frequency of the system, the time duration was increased and the same test was repeated to provide more data points and allow for more accurate and comparative data analyses. Details of the swept-sine tests have been provided in Table 1.

3.2. Seismic ground motion tests

Seismic records of five past devastating earthquakes including 1979 ElCentro, 1999 Kocaeli, 1995 Kobe, 1990 Manjil, and 2011 Christchurch were used for ground motion tests. Records of the selected ground motions were obtained from the Pacific Earthquake Engineering Research Center (PEER), Next Generation Attenuation (NGA-West2) database for historical earthquake records [52], (https://ngawest2.berkeley.edu/). Each record was scaled using SeismoSignal [53] to Peak Ground Acceleration (PGA) values of 0.05g, 0.1g, 0.15g, 0.2g, 0.25g, and 0.3g. Displacement time histories in (mm) were used for each scaled ground motion and were given to the shake table to produce the excitations. A time step of 0.02 s was used for producing time histories using the shake table. Details of each ground motion including event name, station, year, fault type, mechanism, moment magnitude (M_w), PGA, and the dominant frequency (DF) in Hz have been presented in Table 2. Details of conducted ground motion tests can be found in Table 3. All ground motion tests were applied when the tank was full up to 85% of its capacity and each test was repeated up to three times to ensure the accuracy of tests.

4. Simplified mechanical model

A circular cylindrical base-supported fluid tank is considered as shown in Fig. 4.

Laplace's equation for an incompressible, inviscid, and irrotational fluid flow in the polar coordinates, r, θ, and z is expressed as in Eq. (3),

$$\nabla^2 \varphi(r, \theta, z, t) = 0 \tag{3}$$

where φ is the velocity potential of the fluid as a function of time and position. This equation is expanded as Eq. (4),

$$\frac{\partial^2 \varphi}{\partial r^2} + \frac{1}{r}\frac{\partial \varphi}{\partial r} + \frac{1}{r^2}\frac{\partial^2 \varphi}{\partial \theta^2} + \frac{\partial^2 \varphi}{\partial z^2} = 0 \tag{4}$$

To solve this partial differential equation (PDE), a proper set of boundary conditions (BC's) should be considered. There are three main BC's to solve this equation as follows,

$$\begin{cases} BC1: & -\frac{\partial \varphi}{\partial z}|_{z=0} = 0 \\ BC2: & -\frac{\partial \varphi}{\partial r}|_{r=R} = \frac{\partial W}{\partial t} \\ BC3: & (\frac{\partial^2 \varphi}{\partial t^2} + g\frac{\partial \varphi}{\partial z})|_{z=H_l} = 0 \end{cases} \tag{5}$$

where g is the gravitational acceleration and H_l is the distance between the surface liquid and the base. The first boundary condition (BC1)

Table 1
Characteristics of the swept-sine tests.

Observation no.	Tank capacity (%)	Aspect ratio	Frequency band (Hz)	Amplitude (mm)	Duration (s)	Repetition ($No.$)
1	50	2.1	0.1–2.0	5	60	3
2	50	2.1	0.1–2.0	5	120	3
3	50	2.1	0.1–3.0	4	120	1
4	50	2.1	1.0–4.0	1	120	1
5	50	2.1	1.0–4.0	3	120	1
6	50	2.1	2.0–5.0	1	120	1
7	50	2.1	3.0–6.0	0.5	120	1
8	50	2.1	3.0–8.0	0.3	240	1
9	50	2.1	4.0–5.0	0.5	120	1
10	50	2.1	4.0–5.0	0.5	240	1
11	50	2.1	4.0–9.0	0.2	240	1
12	50	2.1	4.0–10.0	0.2	300	1
13	50	2.1	4.0–11.0	0.2	300	1
14	50	2.1	5.5–6.5	0.5	240	1
15	50	2.1	6.0–7.5	0.5	240	1
16	70	2.8	0.1–6.0	0.2	300	3
17	70	2.8	0.1–11.0	0.2	300	3
18	70	2.8	5.0–11.0	0.2	300	3
19	85	3.5	0.1–4.0	0.2	240	1
20	85	3.5	0.1–4.0	0.3	240	2
21	85	3.5	3.0–6.0	0.3	240	1
22	85	3.5	3.0–6.0	0.2	240	2
23	85	3.5	5.0–8.0	0.2	300	1
24	85	3.5	5.0–8.0	0.3	300	1
25	85	3.5	6.0–12.0	0.2	300	1
26	85	3.5	6.0–12.0	0.3	300	1

Table 2
Details of the earthquake records used for seismic ground motion tests of the fluid storage tank.

Event	Station	Year	Fault type	Mechanism	M_w	PGA (g)	DF (Hz)
Imperial Valley	ElCentro	1979	Near-fault, Pulse-like	Strike-Slip	6.53	0.449	0.33
Kocaeli	Atakoy	1999	Far-fault	Strike-Slip	7.51	0.168	0.91
Kobe	KJMA	1995	Near-fault, Pulse-like	Strike-Slip	6.9	0.834	1.45
Manjil	Abbar	1990	Far-fault	Strike-Slip	7.37	0.497	4.53
Christchurch	Cathedral College	2011	Near-fault	Reverse Oblique	6.2	0.478	0.67

Table 3
Characteristics of the ground motion tests.

Observation no.	Ground motion	Tank capacity (%)	Aspect ratio	PGA (g)	Repetition ($No.$)
1	Christchurch	85	3.5	0.05	3
2	Christchurch	85	3.5	0.10	3
3	Christchurch	85	3.5	0.15	3
4	Christchurch	85	3.5	0.20	3
5	Christchurch	85	3.5	0.25	3
6	Christchurch	85	3.5	0.30	3
7	ElCentro	85	3.5	0.05	3
8	ElCentro	85	3.5	0.10	3
9	Kobe	85	3.5	0.05	3
10	Kobe	85	3.5	0.10	3
11	Kobe	85	3.5	0.15	3
12	Kobe	85	3.5	0.20	3
13	Kobe	85	3.5	0.25	3
14	Kocaeli	85	3.5	0.05	3
15	Kocaeli	85	3.5	0.10	3
16	Kocaeli	85	3.5	0.15	3
17	Manjil	85	3.5	0.05	3
18	Manjil	85	3.5	0.10	3
19	Manjil	85	3.5	0.15	3
20	Manjil	85	3.5	0.20	3
21	Manjil	85	3.5	0.25	3

implies zero vertical velocity at the tank base while BC2 represents the radial velocity at the tank wall. The function W in BC2 is the radial deformation of the tank body and is a function of z, θ, and t. This function depends on several factors, the most important of which are the excitation characteristics and flexibility of the tank wall [11], among others. BC3 represents the linear sloshing theory of the surface liquid vibrations. Two modes of vibration for a fluid-tank system under base excitation can be identified, i.e. the impulsive mode and the convective mode. Convective mode represents vibrations of the surface fluid which is independent of the wall flexibility while the impulsive mode reflects the vibrations of the fluid in the lower part of the tank and close to the base which highly depends on the flexibility of the wall. This implies that the velocity potential function of the fluid can be regarded as the sum of two parts of this function for impulsive (φ_{imp}) and convective (φ_{con}) modes as in Eq. (6) when represented in the cylindrical coordinates,

$$\varphi(r,\theta,z,t) = \varphi_{imp}(r,\theta,z,t) + \varphi_{con}(r,\theta,z,t) \tag{6}$$

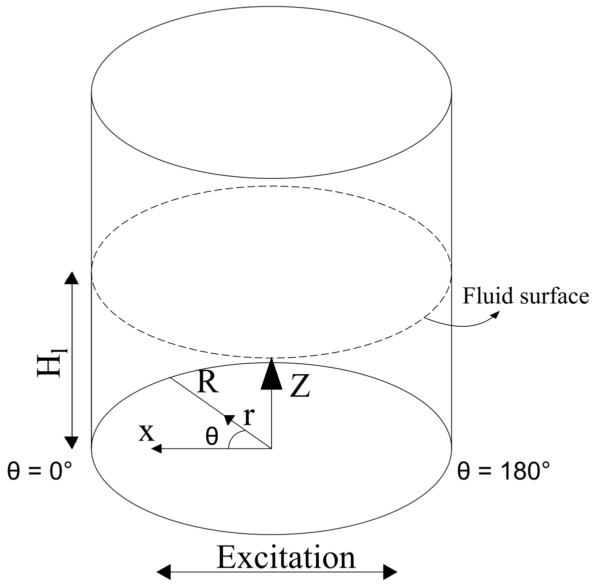

Fig. 4. Fluid flow representation in a circular cylindrical container under base excitations.

Taking into account different boundary conditions at the base, surface fluid, and the tank wall, equations of velocity potential for impulsive mode and convective mode can be obtained, details of which can be found in other Refs. [11,54]. Assuming small amplitude and linearized fluid motions at the fluid surface, the jth cyclic natural frequency of the convective mode is obtained according to Eq. (7),

$$f_{cj} = (\frac{1}{2\pi})\sqrt{\lambda_j \frac{g}{R} \tanh(\lambda_j S)} \tag{7}$$

where λ_j is the jth root of the first derivative of the Bessel function of the first kind of order one ($J_1{}'$). The values of the first three roots of $J_1{}'$, i.e. λ_1, λ_2, and λ_3 are 1.8412, 5.3314, and 8.5363, respectively. g is the gravitational acceleration, S is the aspect ratio, and R is the radius of the tank. Corresponding to each convective mode frequency, there are convective masses and heights. Through applying appropriate BC's for the surface fluid vibrations and solving Eq. (4) for the convective mode, the height of the jth convective mass is formulated as below [11],

$$h_j = [1 - \frac{1}{\lambda_j S} tanh(0.5\lambda_j S)]H_l \tag{8}$$

The velocity potential equation for the impulsive mode highly relates to the flexibility of the wall. Shell flexibility, the flexibility of the base, the thickness of the shell, the direction of ground excitations (horizontal or vertical), and the base fixity conditions are among the factors that affect the boundary conditions required for solving the impulsive velocity potential function. These important factors subsequently affect the closed-form formulas presented for the structural characteristics of the tank including cyclic natural frequencies, masses, and heights of the equivalent lumped masses. The structural characteristics of fluid tanks have been examined by different researchers using various methods such as the FE method, Rayleigh–Ritz method, etc. [55–58]. Recently efforts by various researchers were made to modify the originally proposed equation in this regard [23,59–62]. Here, the fundamental impulsive cyclic natural frequency for a flexible tank is obtained from Eq. (9) [15,54],

$$f_{i1} = \frac{C}{2\pi}\frac{1}{H_l}\sqrt{\frac{E_t g}{\gamma_t}} \tag{9}$$

where E_t is Young's modulus of elasticity of the tank material, g is the gravitational acceleration, γ_t is the density of water, H_l is the height of liquid in the tank, and C is a dimensionless parameter, called "Frequency Parameter" which depends on several factors including aspect ratio (S), the ratio of the thickness of the wall to the radius of the tank ($\frac{t_w}{R}$), E_t, γ_t, and Poisson's ratio of the tank material (ν) [11]. This parameter can be found through charts presented in [11,15,54] and is represented as below,

$$C = \omega_{i1} H_l \sqrt{\frac{\rho_t}{E_t}} \tag{10}$$

which ω_{i1} is the fundamental impulsive circular natural frequency of the tank-water system. The height of the impulsive mass depends on both the aspect ratio (S) and the ratio of the wall thickness to the radius ($\frac{t_w}{R}$) of the tank and has been presented in graphs for the design of tanks [15,54].

5. Experimental results

A sampling rate of 200 Hz with a Nyquist frequency of 100 Hz was used for data acquisition for swept-sine and ground motion tests. Acquired data were analysed in frequency and time–frequency domains based on FFT, PSD, CPSD, and STFT (Spectrogram) analyses using the Signal Processing Toolbox of MATLAB R2023a. These analyses were applied to obtain the natural frequencies and damping ratios of the detected vibrational modes. Furthermore, they were employed to investigate the effect of the frequency content of the input excitation over structural responses of the system including shell accelerations and strain values. Details of conducted data analysis to achieve the aims of this research are elucidated in the below sub-sections.

5.1. Swept-sine tests: Damping ratios and natural frequencies

In total, 38 swept-sine tests with different frequencies ranging from 0.1 Hz to 12 Hz and amplitudes from 0.2 mm up to 5 mm, as described in detail for each test in Table 1, were applied to the tank. Frequency domain and time–frequency domain analyses were conducted over time-history measurements of sensors attached to the tank. The PSD, FFT, and STFT or Spectrogram were calculated for time-history measurements of accelerations, displacements, and strains recorded by the respective sensors. The PSD analyses were conducted using the Autoregressive (AR) spectral density estimate based on the Burg's method [63–66] which applies an AR linear prediction filter to the input signal while constraining the filter parameters to fulfil the Levinson–Durbin recursion [67,68]. Using the applied analyses, natural frequencies of different modes of the vibrations of the coupled fluid-tank system were detected.

The half power bandwidth (−3 dB rule) method [69–71] was used to calculate the damping ratio (ζ) of each detected mode of vibration, and a quality (amplification) factor (Q) was calculated corresponding to each damping ratio. The relationship between the amplification factor, the damping ratio, and the bandwidth are as defined in Eqs. (11) and (12) [69,70],

$$Q = \frac{1}{2\zeta} \tag{11}$$

$$Q \approx \frac{\omega_p}{\omega_2 - \omega_1} \tag{12}$$

where, ω_p is the peak frequency in Hz, and (ω_2 - ω_1) is the bandwidth in Hz corresponding to positions where peak power amplitude (A_{max}) drops for 3 dB which corresponds to positions of the $\frac{\sqrt{2}}{2} A_{max}$. Fig. 5 (a–e) illustrates the power amplitude graph of a series of signals versus the Nyquist frequency f in Hz and F_c is the centre frequency in Hz at which the damping ratio has been calculated using the half-power bandwidth method. The power amplitude graphs of accelerometers No. 2 and 3 for the aspect ratios of 2.1 and 2.8, respectively, and accelerometers No. 2, 7, and 11 for the aspect ratio of 3.5 have been illustrated in Fig. 5 (a–e) for calculations of damping ratios at different frequencies using the half-power bandwidth method. Damping ratios of 0.5% and 3% have been widely used in literature and seismic design codes of fluid

Table 4
Evaluated experimental and theoretical natural frequencies of the thin-walled steel fluid-tank system.

S	Experimentally detected modes (Hz)											Theoretical modes (Hz)		
	1	2	3	4	5	6	7	8	9	10	11	f_{c1}	f_{c2}	f_{i1}
2.1	**1.85**	3.60	5.60	7.20	9.80	14.30	20.20	33.10	35.90	42.50	70.04	1.037	**1.77**	78.11
2.8	–	4.02	5.52	6.50	9.80	14.30	20.30	32.60	36.40	42.30	**56.30**	1.038	1.77	**55.02**
3.5	–	3.70	5.50	6.90	9.60	14.80	19.60	32.70	35.60	**41.66**	77.10	1.038	1.77	**41.51**

storage tanks for the convective and impulsive modes, respectively. The half-power bandwidth analysis conducted over power amplitude graphs of signal measurements at different natural frequencies detected different damping ratios mostly in the range of 0.3%–3%. In Fig. 5 (a, b) damping ratios of 0.3% at the location of the convective mass and 0.4% at the location of accelerometer channel No. 2, both for the centre frequency of 9.5 Hz and the aspect ratio of 3.5, have been calculated. These values fall near the recommended value of 0.5% for the first convective mode. Fig. 5(e) shows a damping ratio of 2.56% at the location of accelerometer channel No. 11 for the centre frequency of 27.70 Hz and the aspect ratio of 3.5 that is a well-matched value to the advised damping ratio of 3% in seismic codes and the literature for analysis and design of stainless steel fluid tanks.

Evaluated natural frequencies and comparisons between theoretical and experimental results have been illustrated in Table 4. In this table, the detected experimental and calculated theoretical natural frequencies have been presented for each aspect ratio (S) examined in this research. For the theoretical modes, the first and second convective modes and the first impulsive mode according to Eqs. (7) and (9), respectively, have been considered. To calculate the fundamental impulsive frequency of the tank-water system, E_t and γ_t for the material of the tank were considered as 200 GPa, and 7850 ($\mathrm{Kg/m^3}$), respectively. Natural frequencies reported in Table 4 are the most frequently observed and dominant frequencies through PSD analysis of signals in almost all sensors for all tests conducted over a specific aspect ratio of the tested fluid storage tank.

Fig. 6 (a, b) shows the PSD graphs versus frequency in Hz illustrated for the acceleration time-history of a series of accelerometers for the aspect ratios of $S = 2.1$ and $S = 2.8$. Examining the experimental results demonstrated that the closest match between the theoretical and experimental convective frequency could be attributed to the aspect ratio of 2.1 that resulted in a frequency of 1.85 Hz which matches the second convective mode frequency f_{c2} according to Eq. (7). For the theoretical impulsive mode of the coupled system, the best matches were found for the aspect ratios of 2.8 and 3.5 for the experimentally detected natural frequencies of 56.30 and 41.66 Hz, respectively. These frequencies match the calculated fundamental impulsive natural frequencies of the fluid tank via Eq. (9). Other observed frequencies from the experimental results were 2.85 Hz for the aspect ratio of 2.1, and 73.30 Hz for the aspect ratio of 3.5. It may be concluded that for the impulsive mode of the system, the higher the aspect ratio the closer the theoretical value to the experimental results. This could be attributed to the fact that the high values of the aspect ratio cause the system to behave more like a flexural beam which corresponds to the theory used for formulating the mathematical model. The discrepancies found between the theoretical and experimentally detected natural frequencies of the coupled fluid-tank system could be attributed to the chaotic, rotational, and highly nonlinear vibrations of the fluid in the tank that violate the simplified hypotheses considered when formulating the SMM of these structures. Observations of fluid surface vibrations during swept-sine tests which demonstrate the nonlinear, rotational, and chaotic fluid surface vibrations have been illustrated in Fig. 7. Based on the experimental results obtained for the natural frequencies of the fluid tank system, it seems that consideration of higher sloshing modes will result in more exact calculations for the analysis and design of fluid storage tanks.

5.2. Effects of the swept-sine excitation characteristics over responses of the system

In this section, the effects of the input excitation's frequency content, amplitude, and duration on the structural responses of the tank-water system including accelerations and axial strains are examined.

First, the swept-sine excitation frequency band and amplitude effects over the PSD intensities of accelerometer Channel Nos. 2 and 3 for the aspect ratios of 2.1 and 2.8 are studied in frequency and time–frequency domains. These channels represent the locations of the impulsive mass for these aspect ratios. The PSD graphs of the accelerometer Channel No. 2 for the aspect ratio of 2.1 has been depicted in Fig. 8 (a–d), while Fig. 9 (a, b) illustrates the spectrogram of accelerometer Channel No. 3 for the aspect ratio of 2.8. Two swept-sine signals with the same duration but different amplitudes and frequency bands were considered for the aspect ratio of 2.1 in Fig. 8(a) containing a frequency window of [17 20.5] Hz in this graph which shows how the amplitude of the PSD is magnified for a frequency of 18.8 Hz when the frequency of the swept is increased from [1 4] Hz to [2 5] Hz even with a lower amplitude. In Fig. 8(b), a frequency of around 33 Hz was the focus of attention. This figure shows two swept-sine signals with the same amplitude and duration but different frequency bands. A frequency window of [30 36] Hz shows that the higher amplitude of the PSD graph occurs under the swept-sine signal with the higher frequency band. Fig. 8(c) and (d) demonstrate the same effects under different frequency bands and amplitudes.

The spectrogram time–frequency representation of a signal is used to demonstrate the variations of the frequency content of a signal over time [72]. The one-sided spectrograms using the STFT method for accelerometer Channel No. 3 for the aspect ratio of 2.8 have been calculated and represented in Fig. 9 (a, b). A kaiser window of length 200 samples with a shape factor of $\beta = 5$, equivalent to a leakage of $l = 87.5\%$, 200 Discrete Fourier Transform (DFT) points, and 100 samples (50%) of overlap between adjoining points were used for calculating the STFT of the signals [73]. As seen in Fig. 9 (a, b), the same frequency range which falls in the frequency band of the input excitation signal shows the strongest beams of light which implies higher intensities of the PSD over these frequencies. For the case of the input signal with the frequency band of [5 11] Hz, the expanding beams of light are more obvious and could be interpreted as activating more natural frequencies of the system.

The effects of increasing the base excitation frequency band over the activation of the natural frequencies of the system through analysis of the strain gauge Channel No. 4 are shown in Fig. 10 (a, b) for the aspect ratio of $S = 3.5$. This sensor was attached to the shell at a distance of 70 mm from the base plate. Fig. 10 (a, b) shows the spectrogram of this channel, in response to two swept-sine signal tests with the frequency bands of [0.1 4] and [6 12] Hz, with the same amplitude of 0.3 mm, and durations of 240 and 300 s, respectively. As seen in this figure the same frequency bands of the input excitation have been activated in the corresponding spectrograms of the strain gauge channel under consideration through showing themselves as the brightest rays of light (higher PSD intensities). In Fig. 10(b) for the excitation with the frequency band of [6 12] Hz, activation of more natural frequencies is evident.

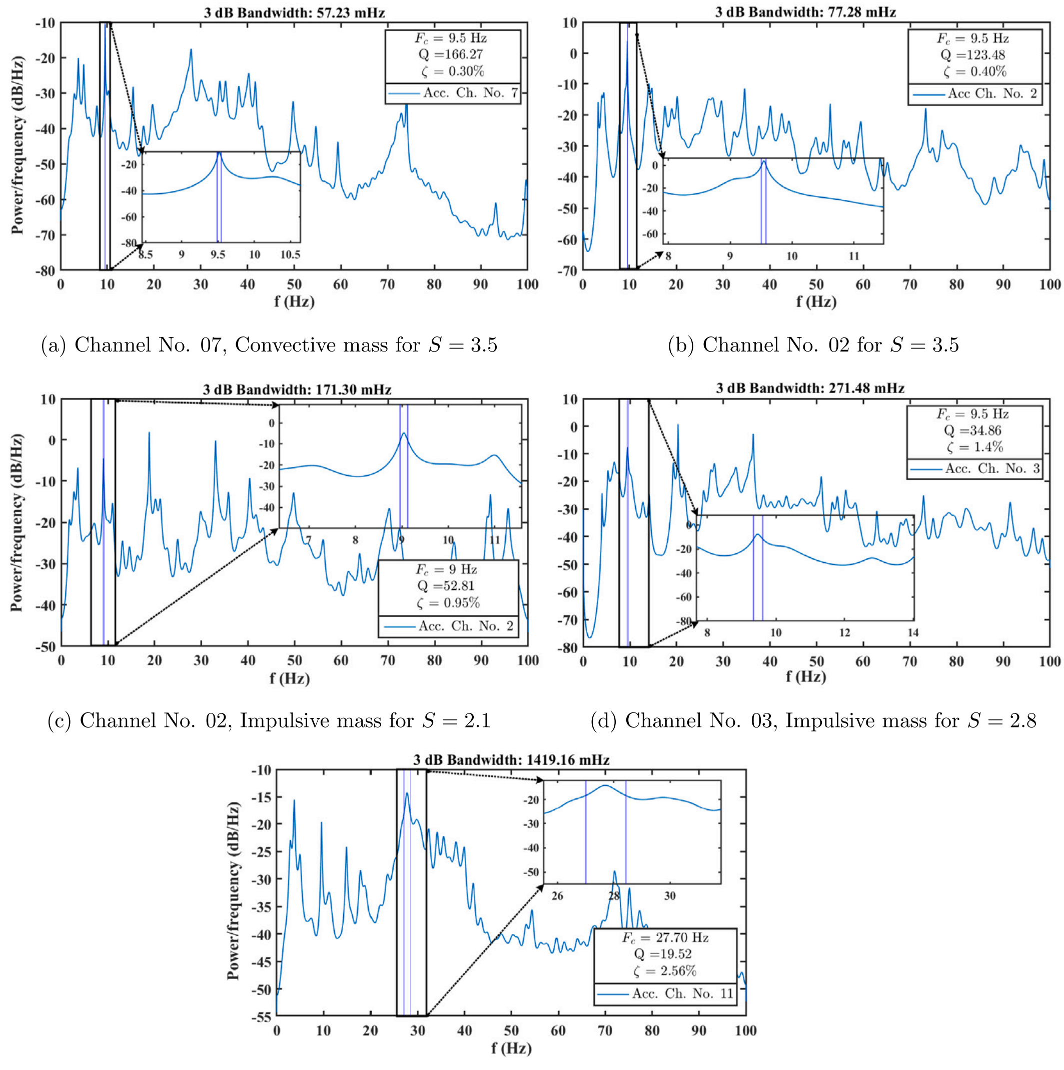

(a) Channel No. 07, Convective mass for $S = 3.5$

(b) Channel No. 02 for $S = 3.5$

(c) Channel No. 02, Impulsive mass for $S = 2.1$

(d) Channel No. 03, Impulsive mass for $S = 2.8$

(e) Channel No. 11, Above water surface for $S = 3.5$

Fig. 5. Power amplitude graph and the calculated damping ratio using half-power bandwidth for different aspect ratios and channels at different locations along the height of the tank extracted from different swept-sine tests.

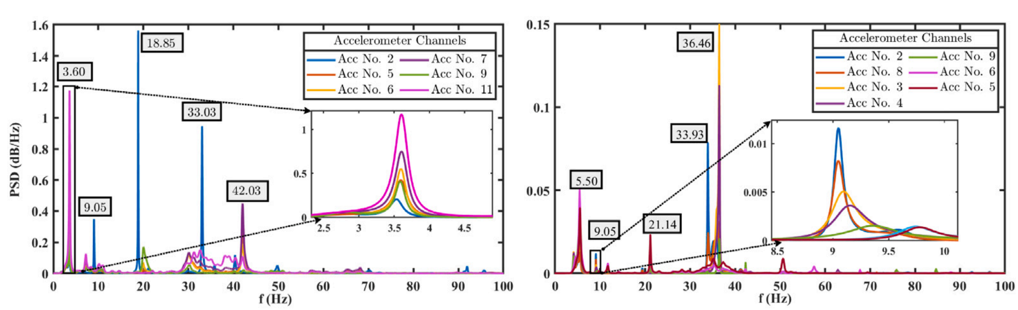

(a) $S = 2.1$

(b) $S = 2.8$

Fig. 6. Power spectral density graph for a series of accelerometer channels: (a) Swept-sine [1 4] Hz, 3 mm amp, 120 s, (b) Swept-sine [0.1 6] Hz, 0.2 mm amp, 300 s.

5.3. Ground motion tests

In this section, the effects of different Near-fault and Far-fault seismic ground motions with different frequency contents have been examined over the structural responses of the steel fluid storage tank. Considered ground motions which were described in detail in Section 3.2 and Table 2 were scaled according to Table 3 and were applied to the shake table when the tank was full up to 85% of its capacity. As discussed before this level of water in the tank is equal to the aspect ratio of 3.5. The effects of these ground motions at different PGA scales over a series of signals have been studied. These

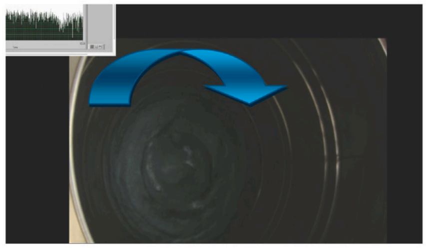

Rotational fluid surface vibrations

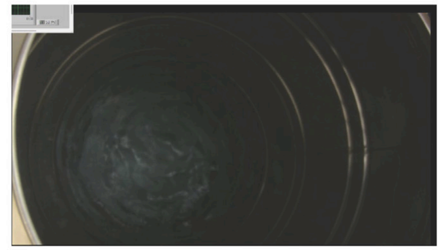

Planar nonlinear fluid surface vibrations

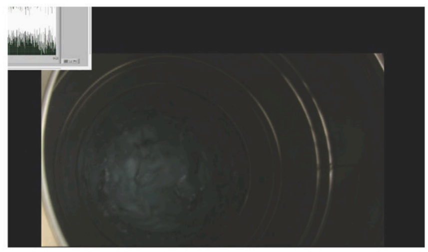

Chaotic fluid surface vibrations

Fig. 7. Observation of fluid surface vibrations during swept-sine excitation tests.

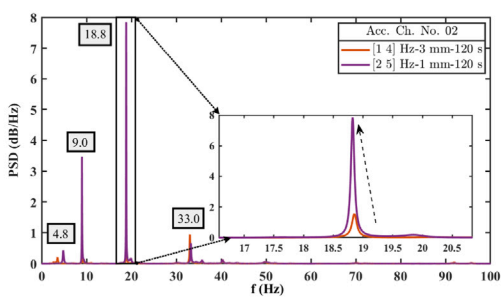

(a) Different frequency bands and amplitudes

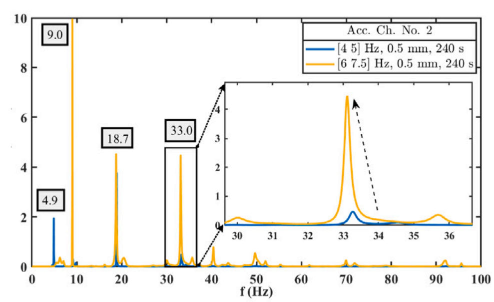

(b) Different frequency bands

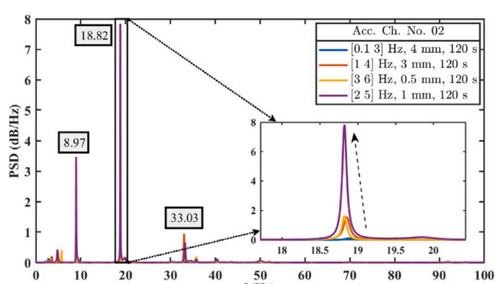

(c) Different frequency bands and amplitudes

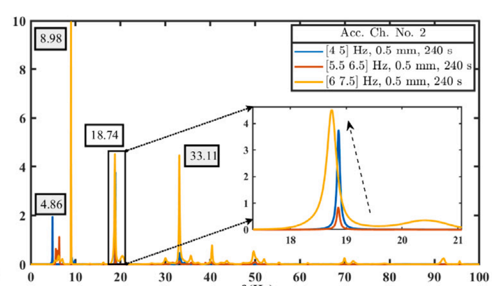

(d) Different frequency bands

Fig. 8. PSD graphs of accelerometer Channel No. 2 (impulsive mass), for swept-sine tests over the tank with $S = 2.1$, demonstrating the effects of frequency bands and amplitudes on the PSD intensities of the natural frequencies.

signals include measurements of strain gauges at the bottom and mid-height of the tank body as well as accelerometers at different levels of height. Amplification of accelerations transmitted to the tank shell at the positions of calculated impulsive and convective masses as well as fluid surface have been calculated and presented in graphs and tables. A comparative study of the effects of the considered ground motions, all at the same PGA level of $0.1g$, over the acceleration amplifications and strains developed in the shell has been presented.

To examine the frequency content of the applied ground motions, the single-sided amplitude spectrum through the FFT method for these ground motions has been depicted in Fig. 11 (a–e) which shows the distribution of the frequencies of these earthquakes over the frequency range of interest in the conducted tests over the system. In this Figure, $|P1(f)|$ is the single-sided amplitude spectrum of the signal plotted versus the Nyquist frequencies f(Hz). Cross Power Spectral Density (CPSD) is the distribution of power per unit frequency which represents the cross-correlation between two signals [74] and has found applications in structural engineering for structural health monitoring and damage detection [75], among others. The CPSD analysis from the input base excitation acceleration (Channel No. 12, shake table accelerometer) to the output shell acceleration at the location of the convective mass (Channel No. 7) has been presented in Fig. 12.

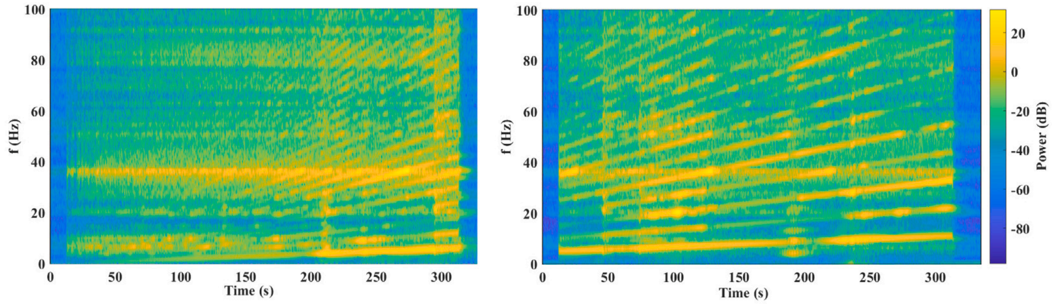

(a) Frequency band of [0.1 6] Hz, 0.2 mm, 300 s (b) Frequency band of [5 11] Hz, 0.2 mm, 300 s

Fig. 9. Spectrogram of accelerometer Channel No. 3 (impulsive mass) for swept-sine tests over the tank with $S = 2.8$, demonstrating the effects of the frequency bands over the PSD intensities at different frequencies.

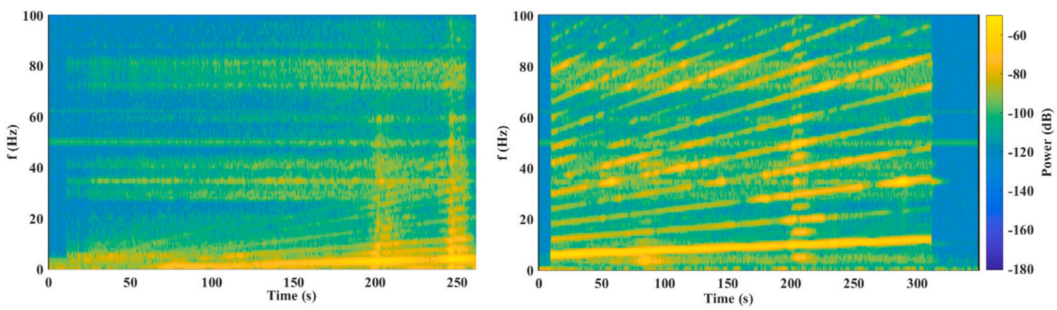

(a) Frequency band of [0.1 4] Hz, 0.3 mm, 240 s (b) Frequency band of [6 12] Hz, 0.3 mm, 300 s

Fig. 10. Spectrogram of strain gauge No. 4 (70 mm from the base) for swept-sine tests over the tank with $S = 3.5$, demonstrating the effects of the frequency bands over the PSD intensities at different frequencies.

The CPSD analysis was conducted using the Welch averaged modified periodogram method of spectral estimation [76] and a Bartlett window with 50% overlap between the adjoining segments. It is inferred from Fig. 12 that the Manjil 0.1g ground motion has the dominant effect over the acceleration time history of the shell at the location of the convective mass over most of the frequency components.

5.3.1. Transmitted acceleration and axial strain in the shell

To examine the effects of the frequency content of the input ground motions on the tested fluid storage tank, the acceleration amplification factor at different heights of the system is calculated and examined according to the below equation [29,77–79],

$$Q_{acc}|_d = \frac{max(|\ddot{u}_d(t)|)}{PIA} \tag{13}$$

where $Q_{acc}|_d$ is the amplification factor of acceleration at a distance of d from the base of the tank, $\ddot{u}_d(t)$ is the acceleration time history of a point over the tank body at a distance of d from the base, and PIA is the absolute value of the peak input acceleration to the system. Acceleration amplification factors for accelerometer Channel Nos. 02, 03, 09, 05, 07, 10, and 11 with distances of 0.38 m, 0.64 m, 0.81 m, 1.2 m, 1.3 m, 1.5 m, and 1.65 m from the base, respectively, under the Manjil 1990 earthquake at different PGA scales have been depicted in Fig. 13 (a). The height of the first convective mass according to Eq. (8) for 85% capacity of the tank ($S = 3.5$), with the water at a level of 1.5 m from the base, is calculated as 1.3 m which corresponds to the location of the accelerometer Channel No. 07. For this water level in the tank, the height of the impulsive mass based on the graphs represented for the design of fluid tanks [15,54] is calculated as 0.81 m which corresponds to the location of accelerometer Channel No. 9. Accelerometer Channel No. 10 is located exactly at the location of surface liquid. Results of the maximum accelerations developed at the selected points on the shell and the calculated acceleration amplification factors under different PGA scales of the Manjil 1990 earthquake have been presented in Table 5. Examining Fig. 13(a) and Table 5 demonstrate that the Manjil 0.1g results in the highest acceleration amplification factors at the levels of the impulsive mass, convective mass, and water surface. Under each PGA scale of this earthquake, the maximum acceleration amplification factor occurs at the water surface. A comparison of variations of acceleration amplification factors at different heights of the shell under different earthquakes, all scaled to the same PGA level of 0.1g, has been illustrated in Fig. 13(b) and the calculated factors have been presented in Table 6. This figure shows that the Manjil earthquake has caused the dominant acceleration amplification factors at most of the levels. Among the considered ground motions at the PGA of 0.1g, the highest acceleration amplification factor at the water surface has occurred under the Kocaeli 0.1g with the DF of 0.91 Hz while the maximum of this factor at the location of the convective mass has occurred under the Kobe 0.1g with the DF of 1.45 Hz. According to Table 2 these two ground motions have the closest DF points to the theoretical convective mode frequencies and the first experimental frequency for the aspect ratio of 2.1 mentioned in Table 4. The Manjil 0.1g with the DF of 4.53 Hz which is the closest value to the first experimental natural frequencies in Table 4 for the aspect ratios of 2.8 and 3.5 has also resulted in similar amplification factors to that of the Kobe 0.1g at the locations of convective mass and water surface. According to Fig. 11, the Manjil 1990 and the Kocaeli 1999 possess higher amplitudes of the $|P1(f)|$ among other earthquakes in the frequency range of [30 40] Hz. Results of Tables 5–6 show that the highest acceleration amplification factors at the location of the impulsive mass have occurred under these two earthquakes. Table 6 shows the amplification of the base acceleration up to 15 times at the fluid surface depending on the applied earthquake. Amplification factors shown in these figures for accelerometer Channel No. 10 at the

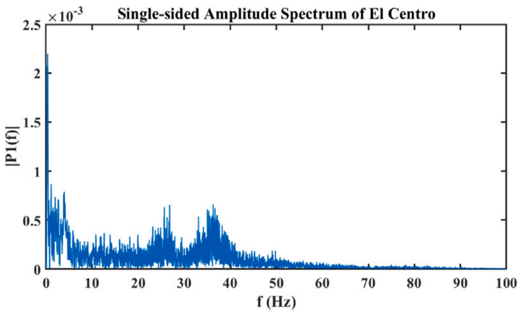

(a) ElCentro

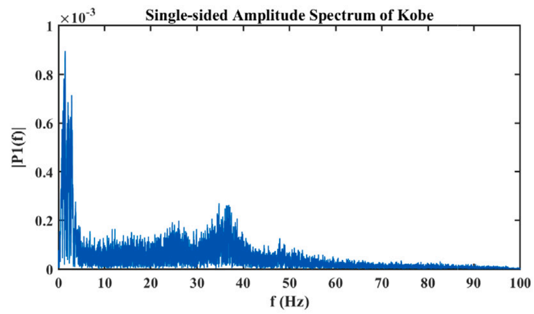

(b) Kobe

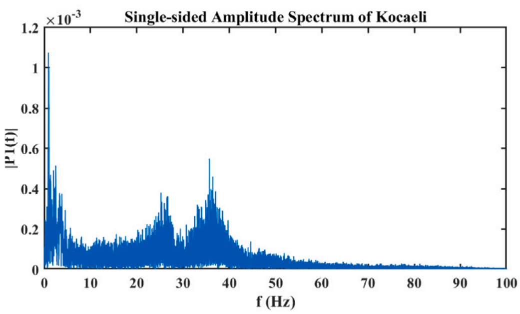

(c) Kocaeli

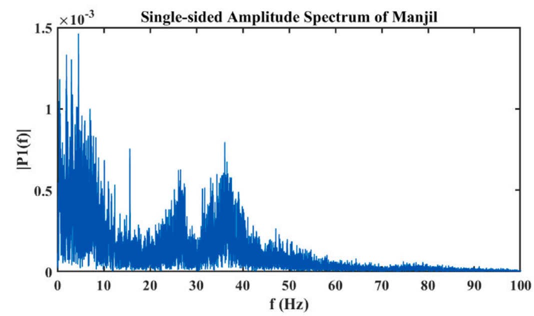

(d) Manjil

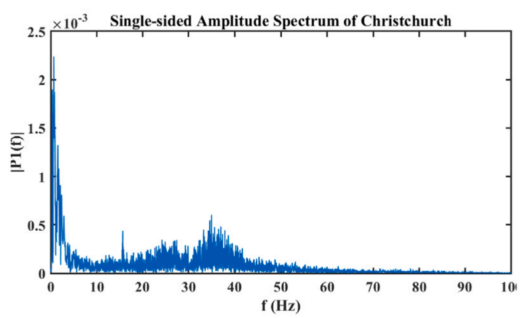

(e) Christchurch

Fig. 11. Frequency content of the selected Far-Fault and Near-Fault ground motions scaled at $0.1g$.

surface fluid reflect higher values than that of accelerometer Channel No. 07 which is the location of the convective mass. This fact confirms that the surface fluid vibrations govern the acceleration responses of the tank body.

The variations of axial strain values over the shell body for strain gauge Channel Nos. 21, 18, and 19 at distances of 70 mm, 320 mm, and 470 mm, respectively, under different PGA scales of the Majil 1990 earthquake, have been shown in Fig. 14(a). A comparison of variations of axial strain values at different heights of the shell under different earthquakes all at the PGA level of $0.1g$ has been represented in Fig. 14(b). As seen in these figures the highest level of strain under all earthquakes occurs at the position of strain gauge Channel No. 21 which is located 70 mm from the base of the tank. This fact justifies the reason for the common elephant foot buckling phenomenon that happens around the base as a result of high-stress concentrations. Examining Fig. 14 (a, b) shows that by increasing the PGA scale of the Manjil 1990, the absolute axial stain values around the base of the tank increase accordingly and the maximum of these values at this location have occurred under the Christchurch $0.1g$. The response time histories of strain gauge Channel Nos. 21 and 18 which are the strain gauges at distances of 70 mm (strain gauge No. 4) and 320 mm (strain gauge No. 1) from the base, under the Kobe 1995 earthquake at the PGA scale of $0.1g$ have been shown in Fig. 15(a) and (b), respectively. The strain values at the base of the tank in Fig. 15(a) show high levels of compression in the shell with an unsymmetrical trend. However, The strain values recorded by the strain gauge No. 1 at the height of 320 mm as shown in Fig. 15(b), represent a symmetrical behaviour of the compression and tension strains. Failure of the tank through the formation of a crack at the base plate during excitation tests under the Christchurch 2011 $0.30g$ has been shown in Fig. 16 which resulted in the collapse of the tank and end of tests. This rupture in the base plate can be attributed to the repetitive uplift of the tank under the seismic base excitations and the extreme effects of the concentration of stress and strain at this location.

6. Conclusions

A thin-walled stainless steel fluid storage tank freely set over a shake table was subjected to different unidirectional base excitations. The

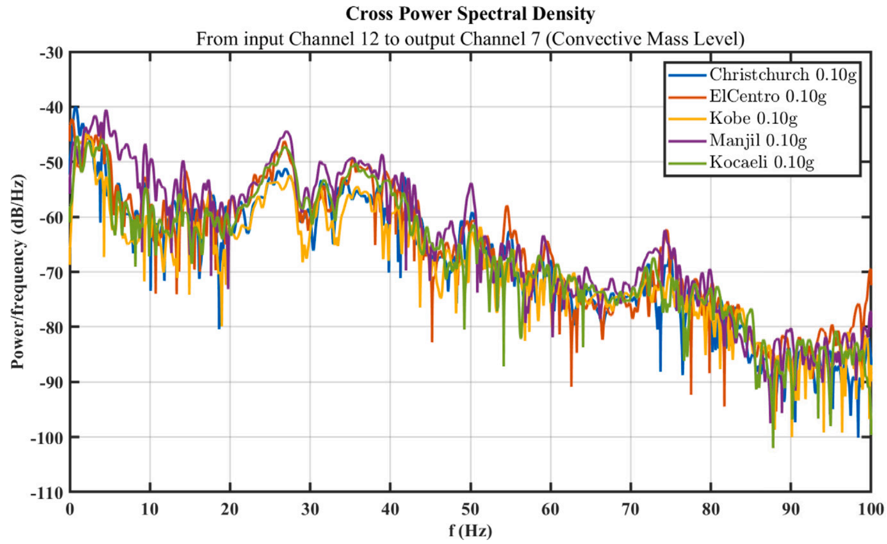

Fig. 12. Comparative evaluation of Cross Power Spectral Density (CPSD) from input base excitation (accelerometer Channel No. 12) to output accelerometer Channel No. 07 (convective mass) for $S = 3.5$ under different earthquakes of $PGA = 0.1g$.

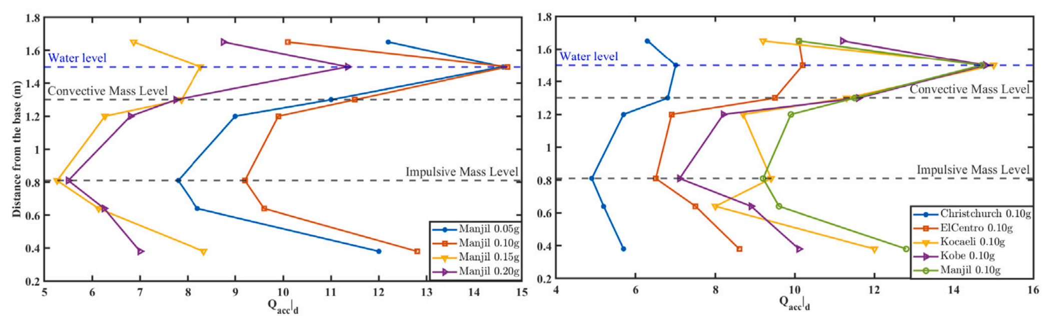

(a) Different PGA scales of Manjil earthquake (b) Different earthquakes all at the PGA of $0.1g$

Fig. 13. Acceleration amplification factor at different heights of the tank body for $S = 3.5$: (a) under different scales of the Manjil 1990 earthquake (b) under five earthquakes all at the PGA of $0.1g$.

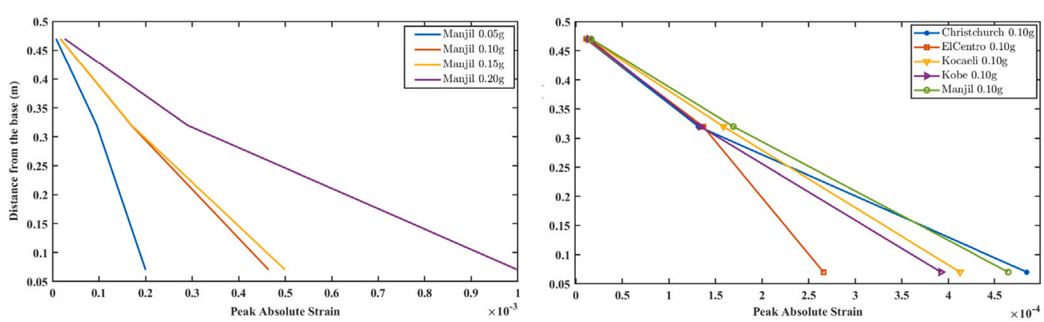

(a) Different PGA scales of Manjil earthquake (b) Different earthquakes all at the PGA of $0.1g$

Fig. 14. Variation of absolute axial strain values on the tank shell along the height for $S = 3.5$: (a) under different scales of the Manjil 1990 earthquake (b) under five earthquakes all at the PGA of $0.1g$.

structural responses of the fluid-tank system under swept-sine input with different frequency bands, amplitudes, and durations were examined. The fundamental natural frequencies of the fluid-tank system were extracted using time–frequency domain analysis based on Power Spectral Density (PSD) analysis and the results were compared with the simplified mathematical formulations widely used in the literature and standards for structural analysis and design of these structures.

The effects of the input excitation frequency content over the structural responses of the system were studied. For the swept-sine excitations which were originally used for the detection of the natural frequencies of the system, each frequency band of the input could activate certain natural frequencies of the system. The higher the range of the frequency band of the input excitation the higher the values of the PSD amplitudes at the studied resonant frequencies and the stronger

Table 5
Amplification of the base excitation acceleration through the shell under different PGA scales of the Manjil 1990 earthquake.

Distance from base (m)	Accelerometer ($No.$)	Location of the sensor	$max(\|\ddot{u}_d(t)\|)$ (g)	$Q_{acc}\|_d$
		$S = 3.5$ $(Slender\ tank), PIA = 0.05g$		
0.38	02	–	0.60	12.00
0.64	03	–	0.41	8.20
0.81	09	***Impulsive mass***	0.39	**7.80**
1.20	05	–	0.45	9.00
1.30	07	***Convective mass***	0.55	**11.00**
1.50	10	***Water surface***	0.73	**14.60**
1.65	11	***Above water surface***	0.61	12.20
		$S = 3.5$ $(Slender\ tank), PIA = 0.10g$		
0.38	02	–	1.28	12.80
0.64	03	–	0.96	9.60
0.81	09	***Impulsive mass***	0.92	**9.20**
1.20	05	–	0.99	9.90
1.30	07	***Convective mass***	1.15	**11.50**
1.50	10	***Water surface***	1.47	**14.70**
1.65	11	***Above water surface***	1.01	10.10
		$S = 3.5$ $(Slender\ tank), PIA = 0.15g$		
0.38	02	–	1.25	8.33
0.64	03	–	0.92	6.13
0.81	09	***Impulsive mass***	0.79	**5.27**
1.20	05	–	0.94	6.27
1.30	07	***Convective mass***	1.18	**7.87**
1.50	10	***Water surface***	1.24	**8.27**
1.65	11	***Above water surface***	1.03	6.87
		$S = 3.5$ $(Slender\ tank), PIA = 0.20g$		
0.38	02	–	1.40	7.00
0.64	03	–	1.25	6.25
0.81	09	***Impulsive mass***	1.10	**5.50**
1.20	05	–	1.36	6.80
1.30	07	***Convective mass***	1.55	**7.75**
1.50	10	***Water surface***	2.27	**11.35**
1.65	11	***Above water surface***	1.75	8.75

Table 6
Amplification of the base excitation acceleration through the shell under different earthquakes with different frequency contents at the same PGA scales.

Distance from base (m)	Accelerometer ($No.$)	Location of the sensor	$max(\|\ddot{u}_d(t)\|)$ (g)	$Q_{acc}\|_d$
		$S = 3.5$ $(Slender\ tank), Christchurch$ 0.10g		
0.38	02	–	0.57	5.70
0.64	03	–	0.52	5.20
0.81	09	***Impulsive mass***	0.49	4.90
1.20	05	–	0.57	5.70
1.30	07	***Convective mass***	0.68	6.80
1.50	10	***Water surface***	0.70	**7.00**
1.65	11	***Above water surface***	0.63	6.30
		$S = 3.5$ $(Slender\ tank)$, *El Centro* 0.10g		
0.38	02	–	0.86	8.60
0.64	03	–	0.75	7.50
0.81	09	***Impulsive mass***	0.65	6.50
1.20	05	–	0.69	6.90
1.30	07	***Convective mass***	0.95	9.50
1.50	10	***Water surface***	1.02	**10.20**
1.65	11	***Above water surface***	1.01	10.10
		$S = 3.5$ $(Slender\ tank), Kocaeli$ 0.10g		
0.38	02	–	1.20	12.00
0.64	03	–	0.80	8.00
0.81	09	***Impulsive mass***	0.94	**9.40**
1.20	05	–	0.87	8.70
1.30	07	***Convective mass***	1.13	11.30
1.50	10	***Water surface***	1.50	**15.00**
1.65	11	***Above water surface***	0.92	9.20
		$S = 3.5$ $(Slender\ tank), Kobe$ 0.10g		
0.38	02	–	1.01	10.10
0.64	03	–	0.89	8.90
0.81	09	***Impulsive mass***	0.71	7.10
1.20	05	–	0.82	8.20
1.30	07	***Convective mass***	1.16	**11.60**
1.50	10	***Water surface***	1.48	**14.80**
1.65	11	***Above water surface***	1.12	11.20

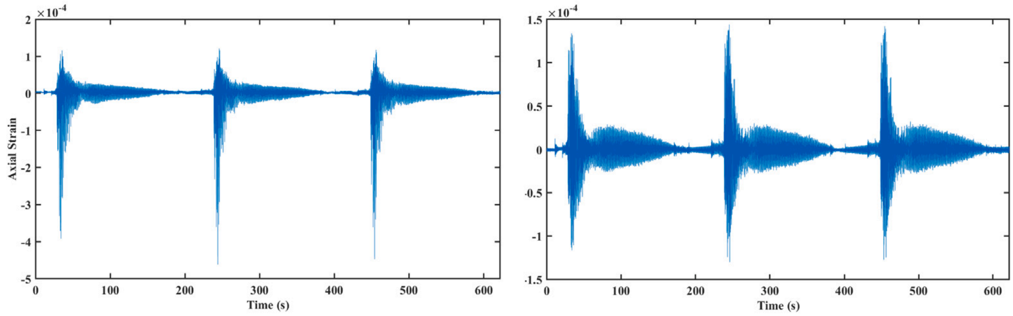

(a) Strain gauge No. 4 at $\theta = 0°$ (b) Strain gauge No. 1 at $\theta = 180°$

Fig. 15. Response time histories of strain gages No. 1 and 4 under the Kobe $0.1g$ earthquake for $S = 3.5$ (three runs of the test): (a) at a distance of 70 mm from the base (b) at a distance of 320 mm from the base.

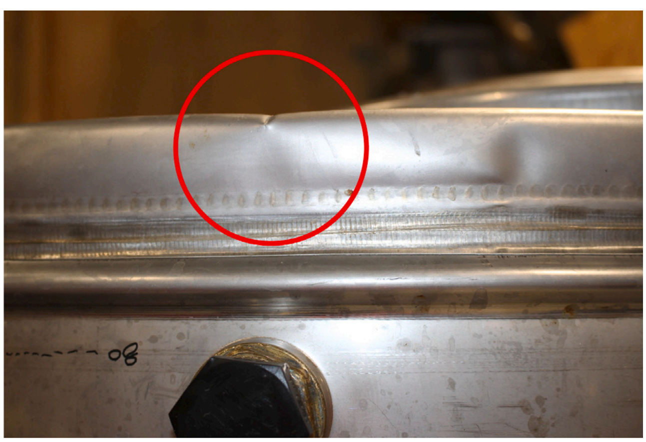

Fig. 16. Crack formation at the base plate during tests under the Christchurch 2011 $0.30g$.

rays reflected in the spectrograms in the frequency range of interest. Since the spectrograms reflect the time-localized frequency content of a signal based on the PSD, the stronger rays in these graphs imply the higher Power values or PSD intensities in (dB/Hz) over the related frequencies and the corresponding time values. Experimental results of the system were examined for five ground motions with different PGA levels, frequency contents, and different fault mechanisms.

The acceleration amplification factor which shows how the input excitation is transferred to the system body at different heights was calculated for different scales of the Manjil 1990 earthquake at different PGA scales at different heights. Also, a comparative study in this regard under different earthquakes, all at the same PGA level of $0.1g$, was conducted. Variations of this factor through the height of the tank showed a nonlinear behaviour with a descending trend from the base of the tank up to the mid-height and then an ascending trend up to the fluid surface. The highest acceleration amplification factor at the fluid surface occurred under the Kocaeli $0.1g$ while the maximum of this value at the location of the convective mass was calculated under Kobe $0.1g$. The maximum values of the acceleration amplification factor at the location of the impulsive mass occurred under Kocaeli $0.1g$ and Manjil $0.1g$, respectively. Frequency domain analysis of these two earthquakes using the single-sided amplitude spectrum approach showed that they possess the dominant high-frequency components over the frequency range of the impulsive mass. This factor again starts decreasing at heights above the fluid surface.

The maximum axial strain values occurred around the base of the tank and decreased in an almost bilinear behaviour at higher levels from the base. Response time histories of strain gauge sensors around the base and the one at a higher level showed high compressive strain values with an unsymmetrical behaviour around the base of the tank (70 mm from the base) and symmetrical tensile-compressive strain values at the strain gauge sensor at a height of 320 mm from the base. A comparative study of the absolute axial strain values developed in the shell under different earthquakes, all at the same PGA level of $0.1g$ was conducted. This study demonstrated that these values are the highest under the Manjil $0.1g$ ground motion, at almost all levels, except for the lowest level of 70 mm from the base at which the maximum of this value occurred under the Christchurch $0.1g$.

Based on the analysed experimental results, it is concluded that,

- The experimentally detected natural frequencies of the tank-water system showed a discrepancy from the theoretical convective ones for aspect ratios of 2.8 and 3.5. The discrepancies found between the theoretical and experimentally detected natural frequencies of the coupled fluid-tank system could be attributed to the chaotic, rotational, and highly nonlinear vibrations of the fluid in the tank that violate the simplified hypotheses considered when formulating the SMM of these structures.
- Experimental results showed the best match between the first experimentally detected natural frequency and the second theoretical convective mode frequency for the aspect ratio 2.1. Therefore, it is considered more conservative to include higher convective vibration modes in the analysis and design of fluid-tank systems.
- For aspect ratios of 2.8 and 3.5, the calculated theoretical fundamental impulsive frequencies of the tank-water system approached the obtained experimental ones, very well. This result can verify the impulsive mode frequency of the fluid-tank system represented by Haroun and Housner [54] based on the flexural beam-like behaviour of the system.
- Accelerations transmitted from the base to the shell non-linearly decrease from the base up to mid-height (location of impulsive mass) and then increase up to the fluid surface. The maximum acceleration amplification factor always occurs at the fluid surface. This factor again starts decreasing from the fluid surface towards higher levels.
- Examining the maximum accelerations transmitted from base to shell under different PGA scales of Manjil earthquake showed the highest acceleration amplification factor at the locations of impulsive mass, convective mass, and water surface under Manjil 0.1g. At each PGA scale of this earthquake, the maximum of this factor occurred at the water surface. Considering the frequency content of the applied ground motions evaluated through FFT and CPSD analyses, the Manjil earthquake showed dominant acceleration amplification factors at most height levels. Comparative studies under different ground motions at the same PGA scales demonstrated the maximum of this factor at the locations of

convective mass and water surface under Kobe 0.1g and Kocaeli 0.1g, respectively. The results of this factor under Manjil 0.1g at the water surface and location of convective mass are very close to that of Kobe 0.1g. These three earthquakes have the closest DF points to the convective mode frequency of the fluid-tank system. The highest acceleration amplification factors at the location of impulsive mass occurred under Kocaeli 0.1g and Manjil 0.1g, respectively, which possess the dominant high-frequency components, among other earthquakes, in the frequency range close to that of impulsive mass.

- Axial strain in the shell decreases from the base towards higher levels with a bi-linear behaviour. Maximum axial strain values occurred around the base of the tank which showed an unsymmetrical behaviour with higher values of compressive strains. This fact justifies the formation of elephant foot bucking as a common type of damage around the base of fluid tanks during earthquakes.
- Frequency content of the input excitation has a considerable effect on the structural responses of the system including accelerations and stains. According to experimental results, higher values of the input excitation frequency range of the swept-sine tests resulted in higher intensities of the PSD and spectrogram graphs of accelerations and axial strains time-histories.
- The damping ratios of 0.5% for the first convective mode and 3% for the first impulsive mode have been recommended in seismic standards and literature for steel fluid storage tanks. The experimental results of the current study demonstrated damping ratios for the detected natural frequencies mostly in the range of 0.3%–3%.
- Detected damping ratios of 0.3% and 0.4% both at a natural frequency of 9.5 Hz, and 2.56% at a natural frequency of 27.70 Hz during experiments fall within close proximity to the widely used values of 0.5% for the first convective mode and 3% for the impulsive mode in seismic standards and research works for analysis and design of tanks.
- Experimental results showed the formation of a crack in the base plate due to repetitive uplift and pounding effects of the base plate under the applied seismic base excitations. Investigations of anchored tanks during past earthquakes have also demonstrated damages to the anchorage system. Therefore, a new flexible energy-dissipating connection to the base for thin-walled stainless steel fluid tanks could offer a more efficient alternative for developing seismic-resilient fluid tanks.

7. Abbreviations

API: American Petroleum Institute
AR: Autoregressive
BC: Boundary condition
BE: Boundary element
CPSD: Cross power spectral density
DFT: Discrete Fourier transform
FE: Finite element
FFT: Fast Fourier transform
FSI: Fluid–structure interaction
NZSEE: New Zealand Society for Earthquake Engineering
PDE: Partial differential equation
PGA: Peak ground acceleration
PIA: Peak input acceleration
PSD: Power spectral density
SMM: Simplified mechanical model
STFT: Short-time Fourier transform

CRediT authorship contribution statement

Seyed Ehsan Aghakouchaki Hosseini: Writing – review & editing, Writing – original draft, Visualization, Validation, Investigation, Formal analysis, Conceptualization. **Sherif Beskhyroun:** Writing – review & editing, Supervision, Resources, Project administration, Methodology, Funding acquisition.

Declaration of competing interest

The authors declare that they have no known competing financial interests or personal relationships that could have appeared to influence the work reported in this paper.

Acknowledgements

Funding: This work was supported by the Earthquake Commission (EQC), Wellington, New Zealand [research grant No. 19/U780] within the Department of Built Environment Engineering, Faculty of Design and Creative Technologies, School of Future Environments, Auckland University of Technology (AUT), Auckland, New Zealand.

References

[1] González E, Almazán J, Beltrán J, Herrera R, Sandoval V. Performance of stainless steel winery tanks during the 02/27/2010 maule earthquake. Eng Struct 2013;56:1402–18.
[2] Rosewitz J, Kahanek C. Performance of wine storage tanks: Lessons from the earthquakes near marlborough. In: Australasian structural engineering conference. ASEC, 2014.
[3] Morris GJ, Bradley BA, Walker A, Matuschka T. Ground motions and damage observations in the marlborough region from the 2013 lake grassmere earthquake. Bull New Zealand Soc Earthq Eng 2013;46(4):169–87, URL https://www.bulletin.nzsee.org.nz/index.php/bnzsee/article/view/173.
[4] Dizhur D, Simkin G, Giaretton M, Loporcaro G, Palermo A, Ingham J. Performance of winery facilities during the 14 november 2016 kaikōura earthquake. Bull New Zealand Soc Earthq Eng 2017;50(2):206–24. http://dx.doi.org/10.5459/bnzsee.50.2.206-224.
[5] Brunesi E, Nascimbene R, Pagani M, Beilic D. Seismic performance of storage steel tanks during the may 2012 emilia, Italy, earthquakes. J Perform Constr Facil 2015;29(5):04014137.
[6] Fischer EC, Liu J, Varma AH. Investigation of cylindrical steel tank damage at wineries during earthquakes : Lessons learned and mitigation opportunities. Pract Period Struct Des Constr 2016;21(3):04016004. http://dx.doi.org/10.1061/(ASCE)SC.1943-5576.0000283.
[7] Team E, et al. Loma prieta earthquake reconnaissance report. Earthq Spectra 1990;127–49.
[8] Housner GW. Earthquake pressures on fluid containers. In: 8th technical report under office of naval research 1954.
[9] Housner GW. Dynamic pressures on accelerated fluid containers. Bull Seismol Soc Am 1957;47(1):15–35.
[10] Haroun MA. Vibration studies and tests of liquid storage tanks. Earthq Eng Struct Dyn 1983;11(2):179–206.
[11] Veletsos AS. Seismic response and design of liquid storage tanks. Guidelines for the seismic design of oil and gas pipeline systems. 1984, p. 255–370.
[12] Malhotra PK, Wenk T, Wieland M. Simple procedure for seismic analysis of liquid-storage tanks. Struct Eng Int 2000;10(3):197–201.
[13] API. Standard API 650: Welded steel tanks for oil storage. Am Petrol Inst Addendum 4 2005.
[14] EN B. Eurocode 8: Design of structures for earthquake resistance- part 4: Silos, tanks and pipelines. European Committee for Standardization Brussels, Belgium; 2006.
[15] NZSEE. Seismic design of storage tanks. New Zealand National Society for Earthquake Engineering; 2009.
[16] Hosseini SEA, Beskhyroun S. Fluid storage tanks: A review on dynamic behaviour modelling, seismic energy-dissipating devices, structural control, and structural health monitoring techniques. In: Structures, vol. 49, Elsevier; 2023, p. 537–56.
[17] Nicolici S, Bilegan R. Fluid structure interaction modeling of liquid sloshing phenomena in flexible tanks. Nucl Eng Des 2013;258:51–6.
[18] Chiba M. Experimental studies on a nonlinear hydroelastic vibration of a clamped cylindrical tank partially filled with liquid. 1993.
[19] Ormeño M, Larkin T, Chouw N. The effect of seismic uplift on the shell stresses of liquid-storage tanks. Earthq Eng Struct Dyn 2015;44(12):1979–96.
[20] Hernandez-Hernandez D, Larkin T, Chouw N, Banide Y. Experimental findings of the suppression of rotary sloshing on the dynamic response of a liquid storage tank. J Fluids Struct 2020;96:103007.

[21] Hernandez-Hernandez D, Larkin T, Chouw N. Shake table investigation of nonlinear soil–structure–fluid interaction of a thin-walled storage tank under earthquake load. Thin-Walled Struct 2021;167:108143.

[22] Fang Z, Chen Z, Yan S, Cao G, Wang J. Dynamic experimental investigation on the uplift response of liquid storage tanks under seismic excitations with different characteristics. Proc Inst Mech Eng C 2013;227(7):1525–34.

[23] Kamarroudi SH, Hosseini M, Hosseini K. Influence of earthquake vertical excitations on sloshing-created P- effect in elevated water tanks: Experimental validation, numerical simulation and proposing a modification for housner model. Eng Struct 2021;246:112995.

[24] Khayat M, Baghlani A, Dehghan SM. A hybrid algorithm for studying the effects of various uncertainties on the nonlinear dynamic responses of steel storage tanks subjected to seismic base excitation. In: Structures. vol. 45, Elsevier; 2022, p. 598–628.

[25] Kang T-W, Yang H-I, Jeon J-S. Earthquake-induced sloshing effects on the hydrodynamic pressure response of rigid cylindrical liquid storage tanks using CFD simulation. Eng Struct 2019;197:109376.

[26] Ogunmakinde OE, Egbelakin T, Omotayo T, Sojobi A. Seismic vulnerability and inventory of at-risk elements in the wine industry: Auckland region case study. In: Structures. vol. 58, Elsevier; 2023, 105346.

[27] Zhang D-Y, Wu J-Y. Experimentally validated numerical analyses on the seismic responses of extra-large LNG storage structures. Thin-Walled Struct 2024;195:111407.

[28] Zhang D-Y, Wu J-Y, Zhou H, Gong M-S. A benchmark shaking table test on the seismic responses of an extra-large LNG storage tank. Earthq Eng Struct Dyn 2023;52(2):439–59.

[29] Liu W, Xiao C, Zhou H, Wang C. Experimental investigation of liquid-tank interaction effects on full containment LNG storage tanks through shaking table tests. Thin-Walled Struct 2023;111527.

[30] Compagnoni ME, Curadelli O. Experimental and numerical study of the response of cylindrical steel tanks under seismic excitation. Int J Civil Eng 2018;16(7):793–805. http://dx.doi.org/10.1007/s40999-017-0218-3.

[31] Ormeño M, Larkin T, Chouw N. Influence of uplift on liquid storage tanks during earthquakes. Coupled Syst Mech 2012;1(4):311–24.

[32] Yazdanian M, Firouzsalari S, Ingham J, Dizhur D. Shake table testing of full scale 22 kl legged liquid storage tank. 2021.

[33] Reyes SI, Almazán JL, Vassiliou MF, Tapia NF, Colombo JI, de la Llera JC. Full-scale shaking table test and numerical modeling of a 3000-liter legged storage tank isolated with a vertical rocking isolation system. Earthq Eng Struct Dyn 2022;51(6):1563–85.

[34] Yazdanian M, Ingham J, Sadashiva V, Cutfield M, Kahanek C, Dizhur D. Seismic fragility curves for stainless-steel wine storage tanks. In: Structures. vol. 33, Elsevier; 2021, p. 4766–80.

[35] Yazdanian M, Ingham JM, Lomax W, Wood R, Dizhur D. Damage observations and remedial options for approximately 1500 legged and flat-based liquid storage tanks following the 2016 kaikōura earthquake. Structures 2020;24(February):357–76. http://dx.doi.org/10.1016/j.istruc.2020.01.024.

[36] Hernandez-Hernandez D, Larkin T, Chouw N. Evaluation of the adequacy of a spring-mass model in analyses of liquid sloshing in anchored storage tanks. Earthq Eng Struct Dyn 2021;50(14):3916–35.

[37] Saka A, Kaya E, Uckan E. Seismic performance of cylindrical liquid storage tanks in the 2023 kahramanmaras earthquakes: A case study of a self-supported oil storage tank. J. Earthq. Eng. 2024;1–12.

[38] Shekari MR, Khaji N, Ahmadi M. A coupled BE–FE study for evaluation of seismically isolated cylindrical liquid storage tanks considering fluid–structure interaction. Elsevier; 2009, URL https://www.sciencedirect.com/science/article/pii/S0889974608000947.

[39] Shekari MR. A coupled BE-FE-BE study for investigating the effect of earthquake frequency content and predominant period on seismic behavior of base-isolated concrete rectangular liquid tanks. J Fluids Struct 2018;77:19–35.

[40] Lee JH, Cho J-R. Simplified earthquake response analysis of rectangular liquid storage tanks considering fluid-structure interactions. Eng Struct 2024;300:117157.

[41] Lee JH, Lee S-H, Han S-W. Nonlinear earthquake responses of unanchored cylindrical liquid storage tanks on flexible soil. In: Structures. vol. 54, Elsevier; 2023, p. 1465–90.

[42] Abd-Elhamed A, Mahmoud S. Seismic assessment of cylindrical storage tanks to records with different frequency contents considering fluid–structure–soil/foundation interaction. J Low Freq Noise Vib Act Control 2024;14613484241275593.

[43] Cui L, Zhu L, Lyu Y, Sun J, Wu Y. Effect of flexible tank wall on seismic response of horizontal storage tank. Processes 2024;12(8):1633.

[44] Kalogerakou ME, Maniatakis CA, Spyrakos CC, Psarropoulos PN. Seismic response of liquid-containing tanks with emphasis on the hydrodynamic response and near-fault phenomena. Eng Struct 2017;153:383–403.

[45] Uckan E, Umut Ö, Sisman FN, Karimzadeh S, Askan A. Seismic response of base isolated liquid storage tanks to real and simulated near fault pulse type ground motions. Soil Dyn Earthq Eng 2018;112:58–68.

[46] Hernandez-Hernandez D, Larkin T, Chouw N. Lid induced sloshing suppression and evaluation of wall stresses in a liquid storage tank including seismic soil-structure interaction. Earthq Eng Struct Dyn 2022;51(11):2708–29.

[47] Mituletu IC, Gillich G-R, Maia NM. A method for an accurate estimation of natural frequencies using swept-sine acoustic excitation. Mech Syst Signal Process 2019;116:693–709.

[48] Wang F, Song G. Bolt early looseness monitoring using modified vibro-acoustic modulation by time-reversal. Mech Syst Signal Process 2019;130:349–60.

[49] Decuyper J, De Troyer T, Tiels K, Schoukens J, Runacres MC. A nonlinear model of vortex-induced forces on an oscillating cylinder in a fluid flow. J Fluids Struct 2020;96:103029.

[50] Sohn H, Lim HJ, DeSimio MP, Brown K, Derriso M. Nonlinear ultrasonic wave modulation for online fatigue crack detection. J Sound Vib 2014;333(5):1473–84.

[51] Matlab S. MATLAB version: 9.14.0 (r2023a). The MathWorks, Natick, MA 2023. URL https://www.mathworks.com.

[52] Ancheta TD, Darragh RB, Stewart JP, Seyhan E, Silva WJ, Chiou BS-J, et al. NGA-West2 database. Earthq Spectra 2014;30(3):989–1005.

[53] Seismosoft. SeismoSignal – signal processing of strong-motion data. 2022, URL https://seismosoft.com/products/seismosignal/ (Accessed 20 June 2022).

[54] Haroun MA, Housner GW. Seismic design of liquid storage tanks. J Tech Counc ASCE 1981;107(1):191–207.

[55] Haroun MA, Ellaithy HM. Model for flexible tanks undergoing rocking. J Eng Mech 1985;111(2):143–57.

[56] Haroun MA, Abou-Izzeddine W. Parametric study of seismic soil-tank interaction. I: Horizontal excitation. J Struct Eng 1992;118(3):783–97.

[57] Haroun MA, Abou-Izzeddine W. Parametric study of seismic soil-tank interaction. ii: Vertical excitation. J Struct Eng 1992;118(3):798–811.

[58] Veletsos A. Seismic effects in flexible liquid storage tanks. In: Proceedings of the 5th world conference on earthquake engineering. vol. 1, Bull Seismol Soc Am McLean, VA, USA; 1974, p. 630–9.

[59] Moradi R, Behnamfar F, Hashemi S. Mechanical model for cylindrical flexible concrete tanks undergoing lateral excitation. Soil Dyn Earthq Eng 2018;106:148–62.

[60] Kazemiyan M, et al. A formula for calculating fundamental natural frequency of partially-filled tanks. Ocean Eng 2019;191:106400.

[61] Rezaiee-Pajand M, Mirjalili Z, Kazemiyan MS. Analytical 2D model for the liquid storage rectangular tank. Eng Struct 2023;289:116215.

[62] Wu J-Y, Yu Q-Q, Gu X-L. A modified analytical model for predicting seismic behaviors of unanchored liquid storage tanks. J Constr Steel Res 2023;208:108018.

[63] Burg JP. Maximum entropy spectral analysis.. Stanford University; 1975.

[64] Orfanidis SJ. Optimum signal processing: an introduction. Macmillan; 1985.

[65] Kay SM. Modern spectral estimation. Pearson Education India; 1988.

[66] Djurić PM, Kay SM. Spectrum estimation and modeling. In: Digital signal processing fundamentals. CRC Press; 2017, p. 375–98.

[67] Stoica P, Moses RL, et al. Spectral analysis of signals. vol. 452, Pearson Prentice Hall Upper Saddle River, NJ; 2005.

[68] Marple Jr. SL. Digital spectral analysis. Courier Dover Publications; 2019.

[69] Papagiannopoulos GA, Hatzigeorgiou GD. On the use of the half-power bandwidth method to estimate damping in building structures. Soil Dyn Earthq Eng 2011;31(7):1075–9.

[70] Casiano M. Extracting damping ratio from dynamic data and numerical solutions. Tech. rep., 2016.

[71] Silvestri S, Mansour S, Marra M, Distl J, Furinghetti M, Lanese I, et al. Shaking table tests of a full-scale flat-bottom manufactured steel silo filled with wheat: Main results on the fixed-base configuration. Earthq Eng Struct Dyn 2022;51(1):169–90.

[72] Boashash B. Time-frequency signal analysis and processing: a comprehensive reference. Academic Press; 2015.

[73] Boashash B. Time-frequency signal analysis and processing: a comprehensive reference. Academic Press; 2016.

[74] Oppenheim AV. Discrete-time signal processing. Pearson Education India; 1999.

[75] Shang Z, Sun L, Xia Y, Zhang W. Vibration-based damage detection for bridges by deep convolutional denoising autoencoder. Struct Health Monit 2021;20(4):1880–903.

[76] Welch P. The use of fast Fourier transform for the estimation of power spectra: a method based on time averaging over short, modified periodograms. IEEE Trans Audio Electroacoust 1967;15(2):70–3.

[77] Chopra AK. Dynamics of Structures: Theory and Applications to Earthquake Engineering. 2nd ed.. Prentice Hall; 2001.

[78] Thomson W, Dahleh M. Theory of vibration with applications. 5ht ed.. Prentice Hall; 1997.

[79] Li J, Chen H-M, Chen J-B. Studies on seismic performances of the prestressed egg-shaped digester with shaking table test. Eng Struct 2007;29(4):552–66.